

Unveiling the charge transfer dynamics regulated by bonding evolution in single-atom Pt/C₃N₅ for boosting hydrogen evolution

Entian Cui ^a, Yulian Lu ^a, Zhaoxia Li ^a, Jingjing Sang ^a, Zhengchao Wang ^b, Minghua Xie ^a, Xiuli Yang ^{a,*}, Jingjing Cao ^{c,*}, Yajun Zhang ^{b,*}

^a Key Laboratory for Advanced Technology in Environmental Protection of Jiangsu Province, Yancheng Institute of Technology, Yancheng, Jiangsu 224051, PR China

^b State Key Laboratory for Oxo Synthesis & Selective Oxidation, National Engineering Research Center for Fine Petrochemical Intermediates, Lanzhou Institute of Chemical Physics, CAS Lanzhou, 730000, PR China

^c College of Chemistry and Chemical Engineering, Lanzhou University, Lanzhou 730000, PR China



ARTICLE INFO

Keywords:

Single-atoms catalysts
Charge migration
Bond evolution
Hydrogen production
Pt/C₃N₅

ABSTRACT

Single-atom catalysts offer a representative platform for heterogeneous catalysis, owing to their maximum atom utilization efficiency and enhanced catalytic performance can be achieved by tuning the local atomic configuration. However, there are rare reports on the charge transfer process and its influence on local atomic configuration during the photocatalytic process. Herein, we for the first time observe the charge migration and bond evolution of a single-atom Pt/C₃N₅ catalysts during the water splitting process by combining synchronous-illumination X-ray photoelectron spectroscopy (SI-XPS) with synchronous-illumination diffuse reflectance Fourier transform infrared spectroscopy (SI-DRIFTS). The results clearly reveal that the dynamic evolution of N-Pt^{δ+} ($0 < \delta < 2$) bond not only provides a real transport channel for the rapid transferring of photo-induced electrons but also suppresses the reverse reaction of forming water from H₂ and O₂. Based on the above unique structure characterizations, single-atom Pt/C₃N₅ catalysts exhibit significantly enhanced hydrogen evolution activity (18.2 mmol·g⁻¹·h⁻¹) under visible light in comparison with metallic Pt-C₃N₅ (3.6 mmol·g⁻¹·h⁻¹).

1. Introduction

Solar-driven photocatalysis has many potential applications including hydrogen evolution, CO₂ reduction, N₂ fixation and organic synthesis [1–4]. Among various reported strategies, heterogeneous catalysts composed of noble metal/semiconductor heterojunction structures are particularly attractive, owing to their combine both the excellent light absorption of semiconductors and unique catalytic properties of noble metal cocatalysts [5,6]. As we all know, the size effect of catalysts intrinsically determines the light absorption ability, charge transfer dynamic and catalytic activity [7–10]. Among them, single-atom catalysts possess superior effective active sites and metal atom utilization efficiency. For instance, single-atom Pt (Pt_S) catalysts can serve as the catalytic centers for promoting charge transfer and boosting hydrogen evolution from water splitting [11–14]. Thus, it is highly desirable to construct highly dispersed and stable single-atom catalysts, which has remained a great challenge.

As a new type of N-rich carbon nitride, C₃N₅ has been proven to be ideal support to coordinate single metal for catalysts [15,16]. The

framework of C₃N₅ is formed by azo-linked graphemic carbon nitride, which will bond metal atoms via azo-linked (-N = N-) over C₃N₅. For the sake of improved photocatalytic efficiency of C₃N₅, various strategies have been carried out, such as exfoliation [17,18], metal deposition [19], and heterojunction [20,21]. As a general chemical exfoliation method, sulfuric acid (H₂SO₄) is most commonly applied in converting the bulk particles into individual nanosheets due to its strong oxidizing power. Specifically, sulfate ions intercalated into the interlayer space of C₃N₅, obtaining the improvement of active sites and charge transport of thin C₃N₅ nanosheets. Recently, a calcination strategy has been developed to anchor isolated metal atoms in the C₃N₅ catalysts [22–25]. For instance, single-atom Co was anchored on C₃N₅ via a calcination process under the nitrogen atmosphere [22]. Similarly, single-atom Co-anchored P-doped C₃N₅ [23], single-atom Ni-anchored C₃N₅ [24], and single-atom Fe-anchored C₃N₅ were all synthesized successfully [25]. Although great efforts have been devoted to improving the activity of C₃N₅, the fundamental understanding of interfacial electronic and bond structure characteristics under the excited state between single-atom and semiconductor has been rarely concerned, and often overlooks the

* Corresponding authors.

E-mail addresses: xlyang@ycit.edu.cn (X. Yang), caojj@lzu.edu.cn (J. Cao), yajunzhang@licp.ac.cn (Y. Zhang).

important underlying mechanism.

Herein, utilizing a combination of synchronous illumination X-ray photoelectron spectroscopy (SI-XPS) with synchronous illumination diffuse reflectance Fourier transform infrared spectroscopy (SI-DRIFTS), we firstly verify that the dynamic evolution of interface N-Pt bonds transforms into N-Pt^{δ+} ($0 < \delta < 2$) bond over single-atom Pt/C₃N₅ catalysts under light excitation. Additionally, this unique interface structure change (N-Pt^{δ+}) can suppress significantly the inverse reaction of water molecule formation from H₂ and O₂. As expected, Pt_{SA}-C₃N₅ catalysts exhibit a record-high H₂ evolution rate of 18.21 mmol g⁻¹ h⁻¹ under visible light irradiation ($\lambda \geq 420$ nm).

2. Experimental section

2.1. Synthesis of Pt single atoms decorated C₃N₅ sheets (Pt_{SA}-C₃N₅ sheets)

2.1.1. Synthesis of bulk C₃N₅

The bulk C₃N₅ was prepared following the previous report [15].

2.1.2. Synthesis of C₃N₅ sheets

A round-bottom flask (50 mL) was placed in an ice bath followed by the addition of 500 mg of the C₃N₅ bulk powder. Next, 50 mL of concentrated H₂SO₄ (65 wt%) was added in the flask very slowly and magnetically stirred for 15 min, then the flask was removed from the ice bath, and the suspension was refluxed at 80 °C for 3 h, resulting in a milky white solution indicative of the nanosheet formation. This sol-type solution was further diluted in deionized H₂O, washed several times to remove any unwanted material, and finally dried in a vacuum oven overnight.

2.1.3. Synthesis of Pt_{SA}-C₃N₅ sheets

Dispersing 50 mg C₃N₅ nanosheet power in 15 mL of distilled water under vigorous stirring, and then 0.13 mL H₂PtCl₆ solution (0.13 mL, 19.3 mmol L⁻¹) was added in the above suspension. The mixture was kept under stirring at 70 °C for 10 h. The resulting product was washed with distilled water and ethanol several times, and was then dried in vacuum at 60 °C overnight, followed by annealing at 125 °C for 1 h in Ar atmosphere.

2.2. Synthesis of Pt nanoparticles-decorated C₃N₅ sheets (Pt_{NP}-C₃N₅)

0.13 mL H₂PtCl₆·6 H₂O (19.3 mmol·L⁻¹) was added into 100 mL aqueous solution containing C₃N₅ nanosheet power, 0.1 mmol L⁻¹ NaOH and 0.1 mmol L⁻¹ NaBH₄. Subsequently, the solution was stirred for 120 min and washed three times with water and ethanol. Finally, the as-obtained sample was dried in the oven at 60 °C.

2.3. Synthesis of Pt single atoms decorated C₃N₄ sheets (Pt-C₃N₄)

2.3.1. Synthesis of C₃N₄

The bulk C₃N₄ was prepared following the previous report [26].

2.3.2. Synthesis of C₃N₄ sheets

The amount of bulk C₃N₄ was put in concentrated sulfuric acid with vigorous stirring for 24 h. Wash it with deionized water until the pH of the supernatant liquid is 7.0. After drying for 12 h, the obtained primary C₃N₄ was further grinded and calcined at 500 °C for 3 h with a heating rate of 5 °C min⁻¹, and obtained C₃N₄ nanosheets.

2.3.3. Synthesis of Pt_{SA}-C₃N₄ sheets

Dispersing 50 mg C₃N₄ nanosheet power in 15 mL of distilled water under vigorous stirring, and then 0.13 mL H₂PtCl₆ solution (0.13 mL, 19.3 mmol L⁻¹) was added in the above suspension. The mixture was kept under stirring at 70 °C for 10 h. The resulting product was washed with distilled water and ethanol several times, and was then dried in

vacuum at 60 °C overnight, followed by annealing at 125 °C for 1 h in Ar atmosphere.

2.4. Characterizations

The morphological characteristics were detected on a field-emission TEM (JEOL JEM-2100 F). The X-ray diffraction (XRD) characterization was carried out on the X-ray diffractometer (Rigaku B/Max-RB, Cu K α radiation). The scientific ESCALAB250i-XPS photoelectron spectrometer was used to record X-ray photoelectron spectroscopy (XPS) spectra and synergism illumination XPS (SI-XPS). The specific surface area was determined by Micromeritics ASAP 2020 M. Photoluminescence spectra (PL) were obtained on a steady-transient state Fluorescence Spectrometer (FluoroMax-4). FTIR test was implemented on Nexus 670 Nicolet Fourier transform infrared spectrometer. UV-Vis DRS characterization was implemented on a HITACHI U-3310 spectrophotometer. The fluorescence decay processes were recorded on an Edinburgh FLS920 phosphorescence system at normal atmospheric temperature. The content of deposited Pt was determined by an inductively coupled plasma-optical emission spectrometer (ICP-OES, OPTIMA8000, USA).

In-situ time-resolved Fourier-transform infrared spectroscopy (ATR-FTIR) of water molecules adsorption was performed using a Bruker Tensor 27 FTIR spectrometer with an MCT detector. The sample was loaded into a cell from HARRIC. Each spectrum was recorded with 32 scans at a resolution of 4 cm⁻¹ under light irradiation.

X-ray adsorption near edge structure (XANES) measurements at Pt LIII-edge of as-prepared samples were measured at the Shanghai Synchrotron Radiation Facility in China. The output beam was selected by Si (111) monochromator. The energy was calibrated by Pt foil. The data were collected at room temperature under fluorescence mode by using the solid-state detector.

Femtosecond pump-probe transient absorption spectrograph measurements (fs-TAS) were performed using a regenerative amplified Ti:sapphire laser system (Coherent; 800 nm, 85 fs, 7 mJ puls⁻¹, and 1 kHz repetition rate) as the laser source and a Helios spectrometer (Ultrafast Systems LLC).

2.5. Photocatalytic H₂ evolution activity measurements

The photocatalytic performances were carried out in a Pyrex top-irradiation reaction vessel connected to a closed gas circulation and evacuation system. H₂ production was performed by dispersing 50 mg as-prepared photocatalysts in an aqueous solution (100 mL) containing triethanolamine (10 vol%) as a sacrificial electron donor. The addition of a phosphate (0.01 M K₂HPO₄) to the reaction system boosted the H₂ generation rate. The reactant solution was degassed several times to remove air prior to irradiation under a 300 W Xenon lamp (PLS-SXE300, PerfectLight Technology Co., Ltd., Beijing). The temperature of the reaction solution was maintained at 20 °C by the flow of cooling water during the reaction. The amount of H₂ production was analyzed using online gas chromatography (Agilent Technologies, 7890 A).

AQY measurement:

The apparent quantum yield (AQY) for H₂ evolution was measured under the same reaction conditions using different monochromatic band-pass filters (420, 450, 500, 550, and 600 nm). The AQY was calculated as follows:

$$\eta_{\text{AQY}} = \frac{2 \times \text{the number of evolvedH}_2}{\text{the number of incident photos}} \times 100\%$$

2.6. Photoelectrochemical (PEC) and Electrochemical (EC) Measurements

All PEC and EC measurements were performed using a CHI 660E electrochemical workstation within a standard three-electrode system, with photocatalyst-coated fluoride-tin oxide (FTO) as the working electrode, a Pt plate as the counter electrode, and Ag/AgCl as a reference

electrode.

Prior to performing these measurements, 20 mg of sample and 50 μL of Nafion were dispersed in 300 μL of isopropanol by 30 min of oscillation. Then, 90 μL of the catalyst colloid was drop-cast onto areas of ca. 1 cm^2 of clean FTO conductive glass plates and dried in air. A 300 W xenon (Beijing Perfectlight Technology Co, Ltd., China) and N_2 -purged 0.5 mol L^{-1} Na_2SO_4 solution were used as the illumination source and electrolyte, respectively. The photocurrent response was measured at a horizontal potential of 1.23 V vs RHE. The electrochemical impedance spectroscopy (EIS) investigation was carried out using the open circuit potential with an alternating current voltage magnitude of 5 mV in the frequency range between 10^{-1} and 10^6 Hz in the dark. Mott-Schottky plots of photocatalysts in N_2 -purged 0.5 M Na_2SO_4 electrolyte (pH 6.8) solution with the same three-electrode system were obtained.

2.7. Computational Details

DFT calculations were carried out based on the Cambridge Serial Total Energy Package. The exchange-correlation energy is described by the generalized gradient approximation using the Perdew-Burke-Ernzerh (PBE) of functional. The effect of the van der Waals interactions is considered by using the empirical correction scheme of Grimme's DFT-D method. A 400 eV plane-wave kinetic energy cutoff was chosen. Geometry optimization has been done with the Brillouin zone sampling limited to the gamma point. The atomic positions were fully relaxed until a maximum energy difference and residual force on atoms, respectively, converged to 10^{-5} eV and $0.03 \text{ eV } \text{\AA}^{-1}$. A 15 \AA vacuum layer was added to prevent the interaction.

2.8. Free energy calculation method

The calculation of free energy was conducted with reference to the previous report [27]. In HER reaction, the proton-electron pair ($\text{H}^+ + \text{e}^-$) participated simultaneously in the reaction. The standard Gibbs free energies of elementary steps, including (i) $\text{H}^+ (\text{aq}) + \text{e}^- + * \rightarrow \text{H}^*$ and (ii) $2 \text{ H}^* \rightarrow \text{H}_2 + 2 *$, were calculated with the reference of standard hydrogen electrode (SHE). The chemical potential relationship between the proton-electron pair and H_2 in the gas phase was first built, and then the free energy of the proton-electron pair can be replaced with the free energy of $1/2 \text{ H}_2$ molecule. Thus, the free energy change of the reaction $\text{HA} \rightarrow \text{A} + \text{H}^+ + \text{e}^-$ can be calculated according to the reaction $\text{HA} \rightarrow \text{A} + 1/2 \text{ H}_2$. Therefore, Gibbs free energy changes of H atom formation (ΔG_1) and H_2 (ΔG_2) molecule formation were calculated as follows:

$$\Delta G_1 = E_{\text{ad}}^{\text{H}} + \frac{1}{2} T \Delta S + eU - kT \ln C_{\text{H}^+} \quad (1)$$

$$\Delta G_2 = -2E_{\text{ad}}^{\text{H}} - T \Delta S + eU - kT \ln P_{\text{H}_2} \quad (2)$$

in which U is the electronic voltage of an excited electron. P_{H_2} is the partial pressure of H_2 in the gas phase. C_{H^+} is the concentration of H^+ in the aqueous solution. The adsorption energy (E_{ad}^{H}) for H_2 was obtained from the DFT calculation at 0 K by the following equation:

$$E_{\text{ad}}^{\text{H}} = E_{\text{H/sur}} - E_{\text{sur}} - \frac{1}{2} E_{\text{H}_2} \quad (3)$$

in which $E_{\text{H/sur}}$, E_{sur} and E_{H_2} are the total energy of the adsorption system, the clean surface and the H_2 molecule, respectively.

3. Results and discussion

3.1. Synthesis and characterizations of Pt single atoms-decorated C_3N_5

In this case, the Pt single atoms-decorated C_3N_5 ($\text{Pt}_{\text{SA}}\text{-C}_3\text{N}_5$) was synthesized via a simple wet chemistry process (Fig. S1). The powder X-ray diffraction (PXRD) pattern of as-prepared samples (Fig. S2) indicates

that only one characteristic 002 peak at 27.5° corresponds to 0.33 nm interplanar sheet distance of C_3N_5 [28,29]. Furthermore, no (100) characteristic peak at $\sim 13.0^\circ$ was detected in the XRD pattern of C_3N_5 , a specific feature of in-plane packing [30,31], indicating distortion in the carbon nitride framework and broadening of the nanochannel distance between heptazine units due to azo ($-\text{N}=\text{N}-$) bridging linkage, in good agreement with the reported literature [15]. Notably, the peak of $\text{Pt}_{\text{SA}}\text{-C}_3\text{N}_5$ slightly shifts to the low-value direction in comparison with that of pure C_3N_5 , indicating that Pt atoms intercalate into the C_3N_5 matrix [32,33]. Transmission electron microscopy (TEM) images (Fig. 1A and S3) show sheet-like structures with lateral sizes up to several micrometers. However, no obvious Pt particle or cluster was observed in C_3N_5 , demonstrating that as-prepared Pt particles were very small in size and uniformly dispersed in the C_3N_5 [34,35]. The element mapping images (Fig. 1B) show the Pt element is homogeneously anchored in the whole nanosheets. Diffuse reflectance spectroscopy (DRIFTS) further investigates the variation of the bond structure of as-prepared catalysts (Fig. S4). Specifically, compared with pure C_3N_5 , the significant enhancement of -C-N- groups in $\text{Pt}_{\text{SA}}\text{-C}_3\text{N}_5$ is observed, on the contrary, the characteristic peaks of -N-C=N-, -N=N-, and -C=N- groups in $\text{Pt}_{\text{SA}}\text{-C}_3\text{N}_5$ obviously decrease. These results indicate the interaction between N atoms with Pt single atoms, which Pt single atoms bonding with adjacent -N-C=N-, -N=N- and -C=N- group (Fig. S5).

To further confirm the characteristics of single-atom Pt, aberration-corrected high-angle annular dark-field scanning transmission electron microscopy (HAADF-STEM) was carried out. As shown in Fig. 1C, the isolated Pt atoms are uniformly dispersed on the C_3N_5 matrix. Subsequently, X-ray absorption fine structure (XAFS) spectroscopy was used to resolve the detailed structural and coordination information [36,37]. The X-ray absorption near edge structure spectra (XANES) of Pt L₃-edge (Fig. 1D) show the different bonding situations of Pt atoms in $\text{Pt}_{\text{SA}}\text{-C}_3\text{N}_5$, Pt foil and PtO_2 . As shown in Fig. 1E, Fourier transforms of the Pt X-ray absorption fine structure (EXAFS) spectra for $\text{Pt}_{\text{SA}}\text{-C}_3\text{N}_5$ contain a prominent peak at 1.51 \AA (Table S1) [38,39], ascribed to the Pt-N contribution. The characteristics metallic Pt-Pt bonding and Pt-O bonding at 2.78 \AA and 1.62 \AA are not observed, respectively, further indicating the single-atom distribution of Pt only interacts with N in C_3N_5 [40]. Furthermore, the corresponding wavelet transform (WT) also exhibits only one intensity maximum at 6.3 \AA^{-1} is attributed to Pt-N coordination, further confirming the atomically dispersed Pt atoms in the obtained sample (Fig. 1F and S6). Additionally, the Pt 4 f XPS spectrum of $\text{Pt}_{\text{SA}}\text{-C}_3\text{N}_5$ (Fig. S7) exhibits a peak located at 71.3 eV (Pt 4 $f_{7/2}$), attributing to the Pt-N bond, which matches well with the Pt^{2+} species [41]. This result is consistent with that of XAFS for $\text{Pt}_{\text{SA}}\text{-C}_3\text{N}_5$. Inductively coupled plasma optical emission spectrometry (ICP-OES) analysis further offers Pt content in $\text{Pt}_{\text{SA}}\text{-C}_3\text{N}_5$ is 0.1 wt%.

3.2. Photocatalytic water splitting reaction

The photocatalytic performances were evaluated by photocatalytic hydrogen evolution from water splitting. Before the activity test, the compared metallic Pt nanoparticles-decorated C_3N_5 ($\text{Pt}_{\text{NP}}\text{-C}_3\text{N}_5$) (Fig. S8) as well as pristine C_3N_5 (Fig. S9) samples were fabricated. As shown in Fig. S10A and S10B, the $\text{Pt}_{\text{SA}}\text{-C}_3\text{N}_5$ (0.1 wt%) catalyst shows relatively higher inherent activity for hydrogen production ($7.2 \text{ }\mu\text{mol}\cdot\text{g}^{-1}\cdot\text{h}^{-1}$) than that of $\text{Pt}_{\text{NP}}\text{-C}_3\text{N}_5$ (0.1 wt%, $1.7 \text{ }\mu\text{mol}\cdot\text{g}^{-1}\cdot\text{h}^{-1}$) in the pure water system, while no evident hydrogen generation could be detected in the pristine C_3N_5 sample. To further investigate the reaction medium need to provide the great potential of $\text{Pt}_{\text{SA}}\text{-C}_3\text{N}_5$ sample for photocatalytic hydrogen evolution. K_2HPO_4 was generally added to the electrolyte as a sacrificial agent [42,43]. As shown in Fig. 2A, a trace amount of hydrogen gas was also detected over pristine C_3N_5 in the K_2HPO_4 system owing to the lack of active sites [44,45], and $\text{Pt}_{\text{NP}}\text{-C}_3\text{N}_5$ catalyst shows the hydrogen evolution rate of $3.6 \text{ mmol}\cdot\text{g}^{-1}\cdot\text{h}^{-1}$. Amazingly, the significant enhancement of hydrogen evolution ability ($18.2 \text{ mmol}\cdot\text{g}^{-1}\cdot\text{h}^{-1}$) was obtained in $\text{Pt}_{\text{SA}}\text{-C}_3\text{N}_5$ under visible light

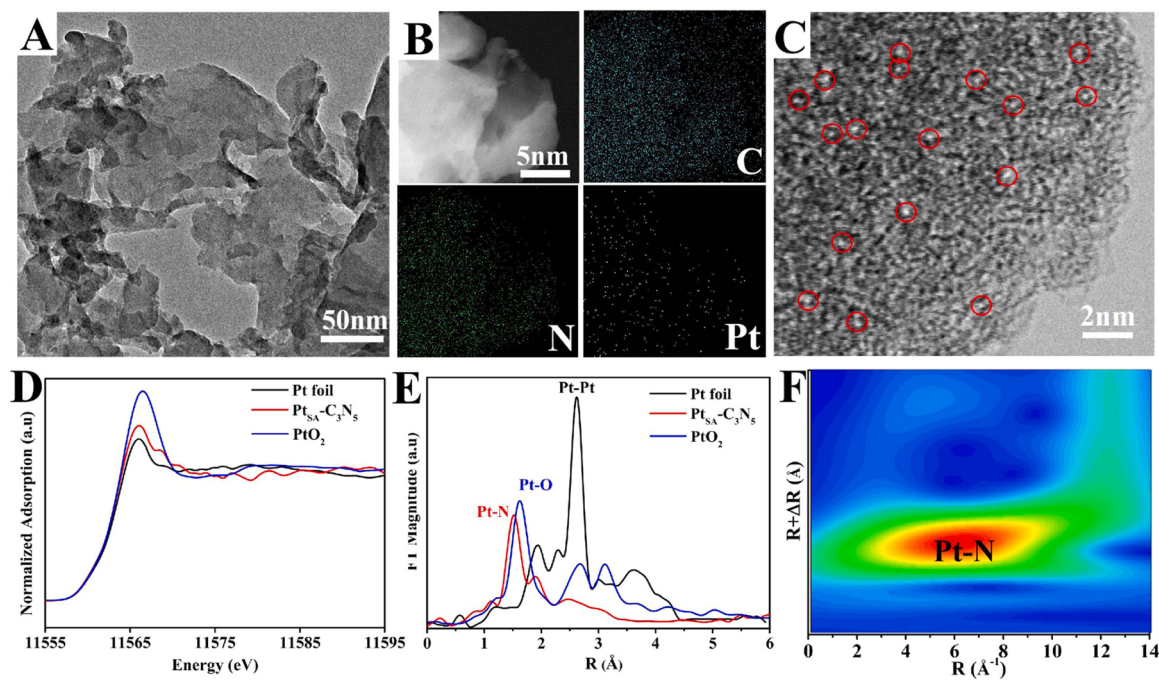


Fig. 1. A) TEM image, B) elemental mapping images and C) Aberration-corrected STEM image of $\text{Pt}_{\text{SA}}\text{-C}_3\text{N}_5$; D) K-edge XANES spectra and E) K_3 -weighted Fourier transform Pt L_{III}-edge EXAFS spectra for $\text{Pt}_{\text{SA}}\text{-C}_3\text{N}_5$, Pt foil and PtO_2 , and F) WT-EXAFS (E) of $\text{Pt}_{\text{SA}}\text{-C}_3\text{N}_5$.

irradiation ($\lambda \geq 420 \text{ nm}$) in K_2HPO_4 solution (Fig. 2A-B), for the reason that HPO_4^{2-} can act as a mediator that directly takes part in the photocatalytic hydrogen production. Similarly, the hydrogen production activities of $\text{Pt}_{\text{SA}}\text{-C}_3\text{N}_4$ (0.1 wt%), Fig. S11 and Table S2) and Pt_{NP} -bulk C_3N_4 (0.1 wt%) in K_2HPO_4 solution are $13.3 \text{ mmol}\cdot\text{g}^{-1}\cdot\text{h}^{-1}$ and $0.16 \mu\text{mol}\cdot\text{g}^{-1}\cdot\text{h}^{-1}$, respectively. By contrast, no or trace amounts of H_2 products are detected in $\text{Pt}_{\text{SA}}\text{-C}_3\text{N}_4$ (0.1 wt%) and Pt_{NP} -bulk C_3N_4 (0.1 wt%) for the pure water system (Fig. S12), respectively. More importantly, the apparent quantum yields (AQYs) of $\text{Pt}_{\text{SA}}\text{-C}_3\text{N}_5$ can also reach up to 37.9% at 450 nm (Fig. 2C). Furthermore, the weight percentage of the Pt loaded to the C_3N_5 was optimized as shown in Fig. S13, and the highest hydrogen evolution activity is obtained on ca. 0.1 wt% $\text{Pt}_{\text{SA}}\text{-C}_3\text{N}_5$. When the Pt atom amount is beyond or below the optimal weight percentage, the effective activity site will decrease, resulting in a decrease of photocatalytic activity. Subsequently, the photocatalytic stability of $\text{Pt}_{\text{SA}}\text{-C}_3\text{N}_5$ was explored in cycling experiments. Fig. 2D shows the hydrogen evolution activity generally remains constant during four cycles, indicating the relatively high photocatalytic stability of $\text{Pt}_{\text{SA}}\text{-C}_3\text{N}_5$ catalysts. After the photocatalytic reaction, the corresponding structure characterizations of $\text{Pt}_{\text{SA}}\text{-C}_3\text{N}_5$ and $\text{Pt}_{\text{SA}}\text{-C}_3\text{N}_4$ were also investigated by the TEM, HAADF-STEM and XAFS analysis. In particular, the high dispersion of Pt single-atom is also observed in the C_3N_5 (Fig. S14A-B) and C_3N_4 nanosheets (Fig. S15A-B), respectively. Additionally, no obvious structural changes were observed in both the XAFS pattern of $\text{Pt}_{\text{SA}}\text{-C}_3\text{N}_5$ (Fig. S14C-D and Table S3) and $\text{Pt}_{\text{SA}}\text{-C}_3\text{N}_4$ (Fig. S15C-D and Table S4) after the reaction. The above results are further verified with the photocatalytic stability of the as-prepared catalyst.

(Photo)electrochemical tests have been also performed, and chronamperometric i-t curves (Fig. S16) clearly reveal that the $\text{Pt}_{\text{SA}}\text{-C}_3\text{N}_5$ catalyst exhibits the highest photocurrent density than pristine C_3N_5 and $\text{Pt}_{\text{NP}}\text{-C}_3\text{N}_5$ catalyst, demonstrating highly efficient photogenerated charge separation and transfer ability over $\text{Pt}_{\text{SA}}\text{-C}_3\text{N}_5$. Electrochemical impedance spectroscopy (EIS) measurements were performed to further clarify the interfacial charge separation as well as the transfer process. According to Nyquist plots (Fig. 2E), the $\text{Pt}_{\text{SA}}\text{-C}_3\text{N}_5$ electrode exhibits a significantly decreased resistance as compared with the pristine C_3N_5 and $\text{Pt}_{\text{NP}}\text{-C}_3\text{N}_5$, indicating enhanced electronic conductivity for

facilitating the charge transport and injection processes [46]. Steady and time-resolved transient photoluminescence (PL) has been performed on the preparation of samples to explore the charge separation and migration capability [47]. Compared with pristine C_3N_5 and $\text{Pt}_{\text{NP}}\text{-C}_3\text{N}_5$, the significantly decreased PL peak of $\text{Pt}_{\text{SA}}\text{-C}_3\text{N}_5$ is obtained in Fig. 2F, demonstrating high charge separation and transfer efficiency through the formation of Pt-N bonding [48]. The transient PL spectra (Fig. 2G and Table S5) indicate that $\text{Pt}_{\text{SA}}\text{-C}_3\text{N}_5$ possesses a higher average lifetime ($\tau_{\text{avg}} = 13.30 \text{ ns}$) than both pristine C_3N_5 ($\tau_{\text{avg}} = 6.91 \text{ ns}$) and $\text{Pt}_{\text{NP}}\text{-C}_3\text{N}_5$ ($\tau_{\text{avg}} = 4.53 \text{ ns}$), respectively, revealing the rapid transferring of photoinduced electrons from C_3N_5 to Pt due to the presence of charge transfer channels (Pt-N bond). More specifically, the first two lifetimes of $\text{Pt}_{\text{SA}}\text{-C}_3\text{N}_5$ at 6.95 and 9.65 ns with 10.41% and 21.23% contributions in the PL decay curve were significantly longer lived in comparison to C_3N_5 and $\text{Pt}_{\text{NP}}\text{-C}_3\text{N}_5$, suggesting that the introduction of azo moiety extends π conjugated network which facilitates better charge carrier mobility on C_3N_5 sheets and prevents faster charge carrier recombination. The third longer lifetime component of 19.55 ns originated due to intersystem crossing (ISC) of the electron from σ^* to π^* orbital followed by radiative relaxation to conjugated π orbital and trap-assisted radiative recombination [15]. Thus, above fast exciton mobility can result in photogenerated electrons to trap sites and recombining by nonradiative processes. Except for PL studies, time-resolved ultrafast transient absorption (TA) spectroscopy was performed to probe the excited-state energy relaxation process and charge-carrier dynamics. Fig. 2H exhibits the negative absorption signals of $\text{Pt}_{\text{SA}}\text{-C}_3\text{N}_5$ in the region of 420–580 nm, attributing to the ground-state bleach and stimulated emission [49,50]. A similar phenomenon is also observed in C_3N_5 and $\text{Pt}_{\text{NP}}\text{-C}_3\text{N}_5$ (Fig. S17). The decay kinetics monitored at 480 nm probe and the fitting parameters are summarized in Table S6. Compared with pristine C_3N_5 ($\tau_1 = 3.96 \text{ ps}$ (51.9%); $\tau_2 = 1031.01 \text{ ps}$ (47.1%)) and $\text{Pt}_{\text{NP}}\text{-C}_3\text{N}_5$ ($\tau_1 = 2.05 \text{ ps}$ (55.7%); $\tau_2 = 852.37 \text{ ps}$ (44.3%)), the transient signal of $\text{Pt}_{\text{SA}}\text{-C}_3\text{N}_5$ can be fitted as $\tau_1 = 1.38 \text{ ps}$ (65.1%) and $\tau_2 = 650.21 \text{ ps}$ (34.9%), indicating that the charge migration ability in $\text{Pt}_{\text{SA}}\text{-C}_3\text{N}_5$ is much higher than those of C_3N_5 and $\text{Pt}_{\text{NP}}\text{-C}_3\text{N}_5$ [51]. The above results further reveal that single-atoms characteristic of $\text{Pt}_{\text{SA}}\text{-C}_3\text{N}_5$ can effectively promote charge

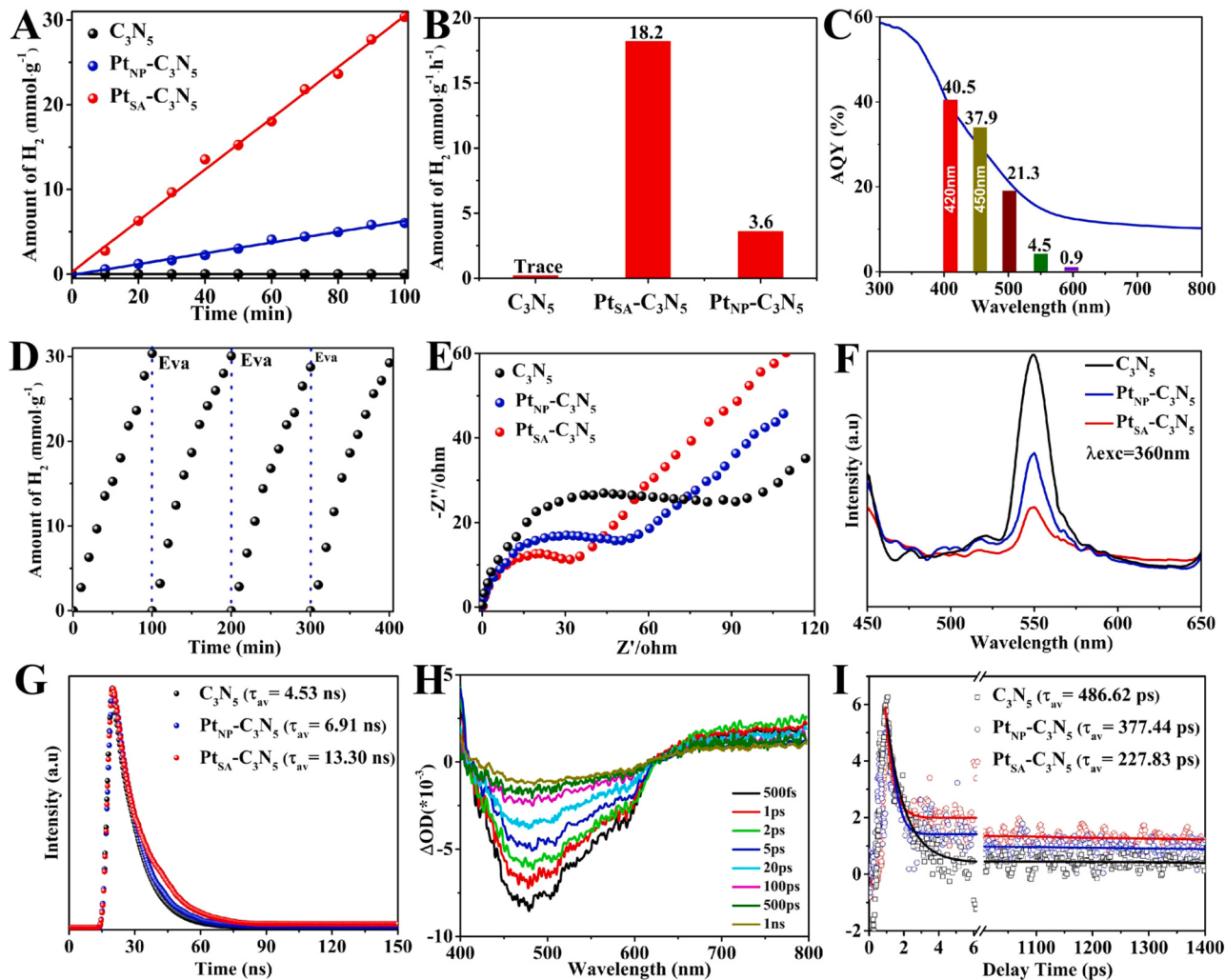


Fig. 2. The photocatalytic H_2 evolution performance under visible light irradiation ($\lambda \geq 420$ nm) (A, B) of pristine C_3N_5 , $Pt_{NP}-C_3N_5$, and $Pt_{SA}-C_3N_5$; AQYs (C) and cycling photocatalytic test of $Pt_{SA}-C_3N_5$ (D). Electrochemical impedance spectroscopy (E), PL (F), time-resolved photoluminescence (TR-PL) spectroscopy (G) of pristine C_3N_5 , $Pt_{NP}-C_3N_5$, and $Pt_{SA}-C_3N_5$. Femtosecond TAS (H) and the Normalized time profiles of transient absorption at 480 nm (I) of $Pt_{SA}-C_3N_5$.

migration and increase hydrogen evolution activity.

3.3. Exploration of the structure evolution during the photocatalytic process

To gain an in-depth understanding on the role of single atoms in catalysis, synchronous illumination X-ray photoelectron spectroscopy (SI-XPS) technique was performed to explore the charge migration and surface chemical state before and after light irradiation [43,52]. In the case of $Pt_{SA}-C_3N_5$ (Fig. 3A), under the dark condition, the main Pt 4 f XPS peak at 71.3 eV was attributed to the Pt-N bond [53], and a small fraction of Pt^0 species (69.9 eV) is also observed. Upon illumination, the Pt-N bonds exhibit blue-shifted in binding energy (BE), revealing the partially positively charged ionic Pt^{+} ($0 < \delta < 2$) in $Pt_{SA}-C_3N_5$ [54]. Notably, the ratio of Pt^{+} to Pt^0 in the Pt region is significantly decreased as compared with the ground state, indicating that Pt^0 species are formed in the excitation states. Meanwhile, the red-shift of C=N-C bond in the N 1 s spectra is also observed (Fig. 3B), which is consistent with that of Pt 4 f spectra. Interestingly, no significant change for bond and charge migration in the C 1 s region (Fig. 3C), indicating that the influence of interface Pt-N bond cleavage on the chemical environment of C atoms may be defused by the extended π -conjugated structure. Moreover, the charge migration and surface chemical state on $Pt_{NP}-C_3N_5$ (Fig. S18) have also been performed by the SI-XPS technique, and the

relatively slight BE of C 1 s, N1s and Pt 4 f peaks can be detected for $Pt_{NP}-C_3N_5$, while no evident changes in the peak shape is observed. These results clearly reveal that the charge separation capability of metallic Pt is much lower than the Pt-N bonding in C_3N_5 , which is consistent with the above photocatalytic hydrogen evolution activity. Moreover, a similar phenomenon about the changes of charge separation and bonding evolution could also be detected in the Pt 4 f, N 1 s and C 1 s region in $Pt_{SA}-C_3N_4$ (Fig. S19). More specifically, under the ground state, the two peaks of 69.8 and 71.3 eV can be assigned to Pt^0 and Pt-N bonds, respectively. Under light irradiation, the partially Pt-N bond cleavage to form a Pt^0 species and binding energy offset of Pt 4 f and N1s peaks are also observed. The above demonstrates further verify that, as compared with metallic Pt nanoparticles, the spatial confinement effects (Pt-N coordination) can effectively promote the anchoring of single-atom Pt over C_3N_5 in the excitation state [22].

In addition to SI-XPS characterization, the synchronous illumination diffuse reflectance Fourier transform infrared spectroscopy (SI-DRIFTS) was also performed to detect the bonding change over $Pt_{SA}-C_3N_5$. As shown in Fig. 3D and Fig. S20, the peaks of -N-C=N- (1628 cm^{-1}) and -C=N- (1481 cm^{-1}) for $Pt_{SA}-C_3N_5$ have been significantly increased under the light irradiation, while the peak of -C-N- (1325 cm^{-1}) decreased obviously. However, no obvious changes on the -N=N- (1426 cm^{-1}) bond can be detected for $Pt_{SA}-C_3N_5$. These results indicate the $Pt-N_2$ and $Pt-N_3$ bonds cleaved and the N_1-Pt^{2+} interface bond is in-

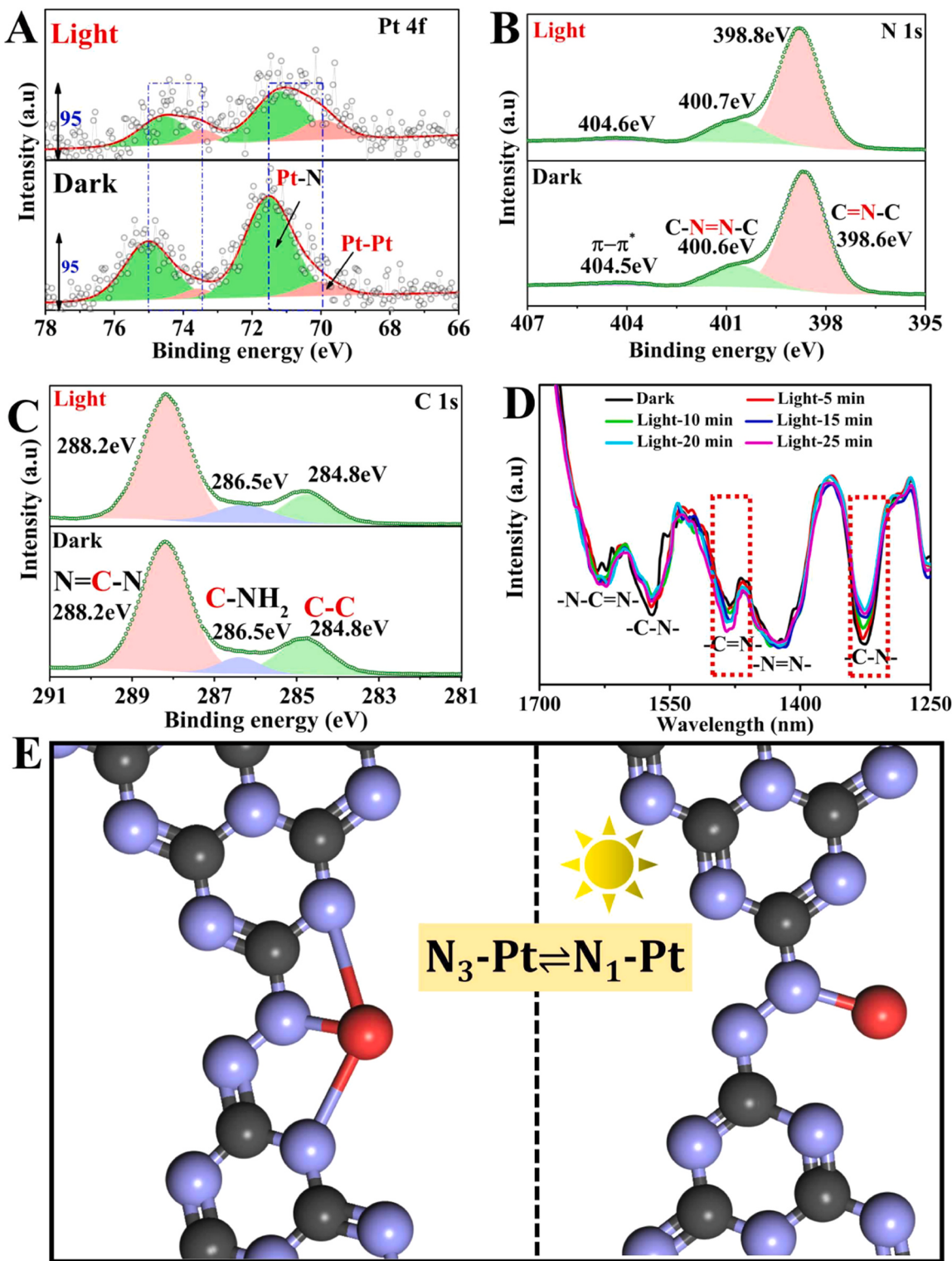


Fig. 3. SI-XPS high-resolution Pt 4 f (A), N 1 s (B), C 1 s (C) spectra of $\text{Pt}_{\text{SA}}\text{-C}_3\text{N}_5$ (with the same horizontal axis), (D) SI-DRIFTS result of $\text{Pt}_{\text{SA}}\text{-C}_3\text{N}_5$; (E) Illustration of structure evolution and electron transport on $\text{Pt}_{\text{SA}}\text{-C}_3\text{N}_5$ under light illumination.

situ transferred into the $\text{N-Pt}^{\delta+}$ ($0 < \delta < 2$) interface bond (Fig. 3E), which further verifies the above results of SI-XPS. The reserved $\text{N-Pt}^{\delta+}$ bonds provide a real transport channel for rapid electron transferring, therefore, $\text{Pt}_{\text{SA}}\text{-C}_3\text{N}_5$ has a more efficient photoinduced electron transferring ability.

To further reveal the influence of surface chemical state changes on photocatalytic hydrogen evolution activity. The hydrogen oxidation

reaction (HOR) over as-prepared samples has also been studied. Prior to the pure water splitting experiment, 2 mL H_2 and 1 mL O_2 were pre-injected into the closed reactor. Under the dark conditions, the H_2 and O_2 amount in the $\text{Pt}_{\text{NP}}\text{-C}_3\text{N}_5$ quickly decreased, while this phenomenon was negligible in the $\text{Pt}_{\text{SA}}\text{-C}_3\text{N}_5$ system and the gas amount remained constant (Fig. 4A). Under light irradiation, the H_2 and O_2 gas evolution amount significantly increased over $\text{Pt}_{\text{SA}}\text{-C}_3\text{N}_5$, whereas, the amount of

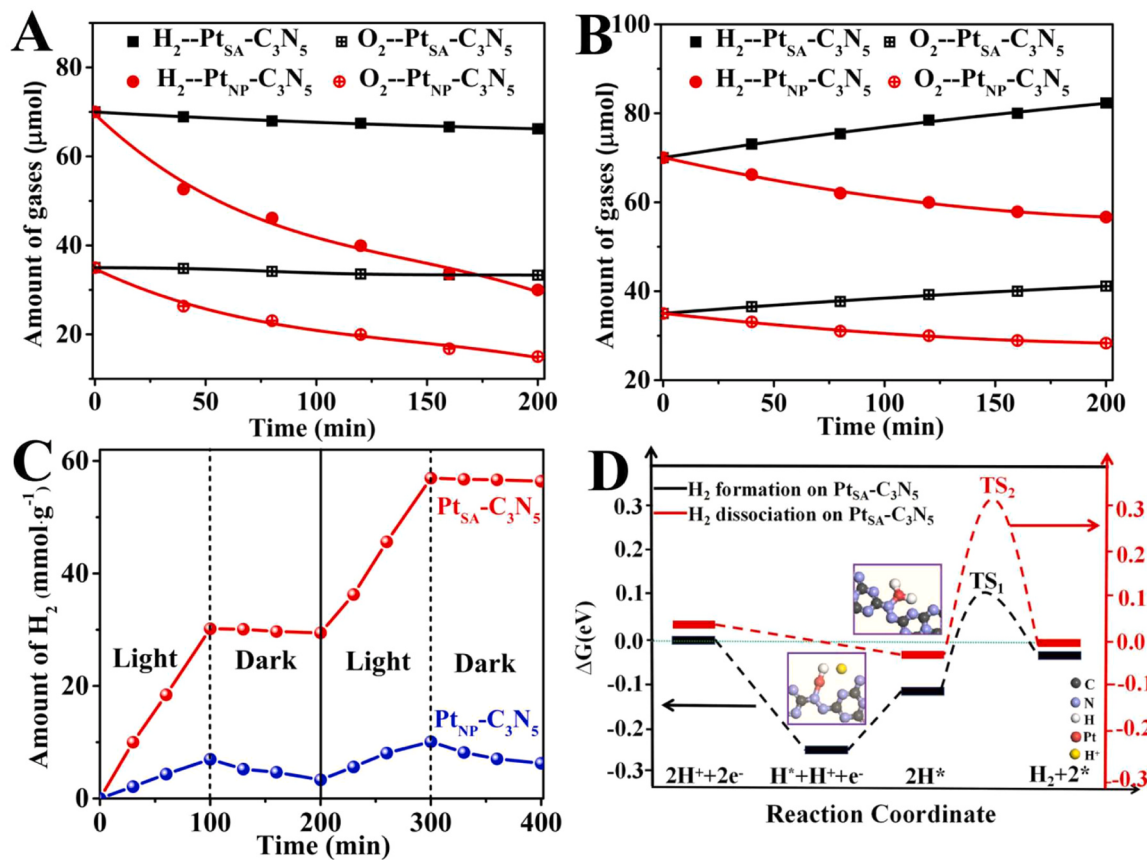


Fig. 4. Reaction time profiles of the HOR with H₂ and O₂ on Pt_{SA}-C₃N₅ and Pt_{NP}-C₃N₅ in pure water system under dark (A) and visible light irradiation ($\lambda \geq 420$ nm) (B); The photocatalytic H₂ evolution activities of Pt_{NP}-C₃N₅ and Pt_{SA}-C₃N₅ with oxygen atmosphere under light irradiation ($\lambda \geq 420$ nm) and followed dark condition (C); Standard Gibbs free energy of HER and HOR in aqueous solution on Pt_{SA}-C₃N₅ (D).

H₂ and O₂ in Pt_{NP}-C₃N₅ system remains decreased (Fig. 4B). These results clearly reveal that Pt_{NP}-C₃N₅ can facilitate the undesirable HOR occurrence, while Pt_{SA}-C₃N₅ exhibits negative activity for the hydrogen-oxidation recombination reaction into H₂O [55,56]. Additionally, the HOR activity of both Pt_{SA}-C₃N₅ and Pt_{NP}-C₃N₅ was also studied in TEOA aqueous solution with O₂ atmosphere. As shown in Fig. 4C, the significant enhancement of H₂ evolution ability is obtained in Pt_{SA}-C₃N₅ under light conditions in comparison with that of Pt_{NP}-C₃N₅. Interestingly, when light irradiation was removed, the amount of H₂ on the Pt_{NP}-C₃N₅ catalysts decreased, yet those on Pt_{SA}-C₃N₅ catalysts decreased negligibly, which is consistent with the results of pure water splitting. Then, the density functional theory (DFT) calculation was performed to reveal the standard Gibbs free energy (ΔG) of HER and HOR on Pt_{SA}-C₃N₅ in the aqueous solution. As shown in Fig. 4D, the stage of H₂ formation, all the values of ΔG are negative, indicating that these processes are exothermic and spontaneous reactions. Compared with H₂ formation, the value of ΔG increases evidently for H₂ dissociation, indicating that the H₂ dissociation is more difficult than H₂ formation on Pt_{SA}-C₃N₅ [35, 57]. Interestingly, in the case of Pt_{NP}-C₃N₅ (Fig. S21), the ΔG value of H₂ dissociation is lower than H₂ formation, demonstrating that the H₂ dissociation is easier than H₂ formation over Pt_{NP}-C₃N₅.

Subsequently, their bandgaps were explored by UV-vis diffuse reflectance spectra (UV-vis DRS). As shown in Fig. S22A and B, the bandgap of C₃N₅ is \sim 1.78 eV. Then, the valence band (VB) of pristine C₃N₅ and Pt/C₃N₅ was measured by ultraviolet photoelectron spectroscopy (UPS), as shown in Fig. S22C. According to the UPS spectra, the VB maximum (E_{VBM} vs NHE) could be calculated via the following equation:

$$E_{VBM} \text{ vs NHE} = 21.22 - E_2 + E_1 - 4.44.$$

For C₃N₅, the E₂ and E₁ are 17.53 and 1.67 eV, respectively.

Therefore, the calculated E_{VBM} vs NHE is 0.92 eV, which is very close to the value obtained from VB XPS spectra (0.93 eV, Fig. S22D). Correspondingly, the conduct band (CB) is -0.85 eV. Correspondingly, the CB and VB of Pt_{SA}-C₃N₅ are -0.86 and 0.89 eV. Based on the calculated values, the band structures of C₃N₅ and Pt_{SA}-C₃N₅ are depicted in Fig. S22E.

3.4. Insight into the H₂ production mechanism

To further discover the significant role of Pt single-atom during the hydrogen evolution process, the corresponding optimal structure of as-prepared catalysts was first calculated. As shown in Fig. 5A and Fig. S23, five structural models of Pt_{SA}-C₃N₅ are constructed. According to the energy minimum principle, the adsorption configuration model of Pt(N₃-1) is the most stable structure due to its lowest adsorption energy (-5.21 eV). Specifically, the bond lengths of Pt (N₃-1) are 1.89 (Pt-N₁ bond), 2.09 (Pt-N₂ bond), and 2.23 (Pt-N₃ bond) Å, respectively. The optimal structure of the reconstructed Pt-N bond over Pt_{SA}-C₃N₅ was also investigated in Fig. 5B. Compared with Pt-N₂ (-1.94 eV) and Pt-N₃ (-1.87 eV), Pt-N₁ (-2.25 eV) exhibits the shortest bond length, indicating Pt-N₁ bond can exist stably in the Pt_{SA}-C₃N₅ catalyst. Furthermore, the different charge density and electronic location functions were simulated over Pt_{SA}-C₃N₅ and Pt-N₁ [58]. As shown in Fig. S24A and B, compared with Pt_{SA}-C₃N₅, the changes in the charge density distribution of Pt-N₁ indicate charge accumulation on the Pt site. Specifically, the charge transfer increases from 0.126 e to 0.172 e after Pt-N₂ and Pt-N₃ cleaved. Then, electronic location functions (ELFs) were also calculated to uncover the evolution of local atomic configuration (Fig. S24C and D). After the cleavage of Pt-N₂ and Pt-N₃ bonding, the position-dependent ELF in Pt-N₁ is close to 0.3 in comparison with

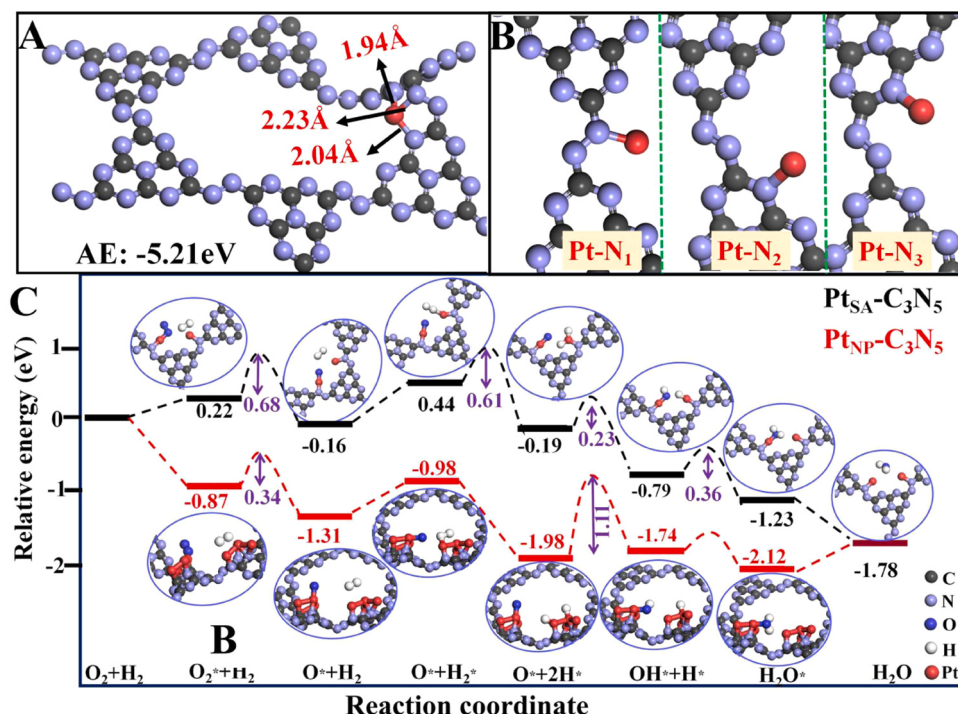


Fig. 5. The calculated model of $\text{Pt}(\text{N}_3\text{-}1)$ (A) and the corresponding reconstructed structure (B) in single atom $\text{Pt}/\text{C}_3\text{N}_5$; (C) Standard Gibbs free energy profile of the reaction between H_2 and O_2 on $\text{Pt}_{\text{NP}}\text{-C}_3\text{N}_5$ and $\text{Pt}_{\text{SA}}\text{-C}_3\text{N}_5$ in the gas phase.

$\text{Pt}_{\text{SA}}\text{-C}_3\text{N}_5$ (0.5), manifesting that the electron distribution is mainly concentrated in the $\text{Pt}-\text{N}_1$ site, which is consistent with the charge density distribution results. Thus, the existence of $\text{Pt}-\text{N}_1$ is regarded as a charge transfer tunnel at the atomic level, which is conducive to rapid photoelectron transfer. Subsequently, the full reaction pathways of HOR reaction over $\text{Pt}_{\text{SA}}\text{-C}_3\text{N}_5$ and $\text{Pt}_{\text{NP}}\text{-C}_3\text{N}_5$ were investigated, respectively. As shown in Fig. 5C and Table S7, the adsorption and dissociation of O_2 and H_2 are thermodynamically favored on $\text{Pt}_{\text{NP}}\text{-C}_3\text{N}_5$ with energy barriers of 0.34 eV and self-dissociation, respectively [59]. However, the adsorption and dissociation of O_2 and H_2 are kinetically hindered on $\text{Pt}_{\text{SA}}\text{-C}_3\text{N}_5$, owing to the high barrier for the O-O bond (0.68 eV) and H-H bond (0.61 eV) [60]. These results further indicate that H^* and O^* species are difficult to form on the $\text{Pt}_{\text{SA}}\text{-C}_3\text{N}_5$ in comparison with $\text{Pt}_{\text{NP}}\text{-C}_3\text{N}_5$. Thus, these theoretical results are highly consistent with the above performance results, and the enhanced hydrogen evolution ability mainly originates from the dynamic bond evolution of Pt species over $\text{Pt}_{\text{SA}}\text{-C}_3\text{N}_5$ catalysts.

4. Conclusions

In summary, the photo-excited dynamic bond evolution and charge migration between single-atom Pt and C_3N_5 have been verified by a combination SI-XPS with SI-DRIFTS. The related results clearly reveal that the dynamic evolution of $\text{N}-\text{Pt}^{3+}$ ($0 < \delta < 2$) bond can significantly promote charge migration. Benefiting from these unique structure features, the $\text{Pt}_{\text{SA}}\text{-C}_3\text{N}_5$ catalysts show the significant enhancement of H_2 evolution ability under visible light irradiation and the effective suppression of HOR under the ground state. This work provides dynamic bond change insights to study the single-atom catalyst in the hydrogen evolution process, which may promote the development of highly efficient photocatalysts for practical solar conversion.

CRediT authorship contribution statement

Cao Jingjing: Resources, Conceptualization. **Yang Xiuli:** Resources, Funding acquisition. **Xie Minghua:** Resources. **Wang Zhengchao:** Data

curation. **Sang Jingjing:** Investigation. **Li Zhaoxia:** Investigation. **Lu Yulian:** Investigation. **Cui Entian:** Writing – original draft, Investigation. **Zhang yajun:** Writing – review & editing, Validation, Supervision, Funding acquisition, Conceptualization.

Declaration of Competing Interest

The authors declare that they have no known competing financial interests or personal relationships that could have appeared to influence the work reported in this paper.

Data Availability

Data will be made available on request.

Acknowledgements

This work was supported by the National Natural Science Foundation of China (22072168, 22171239, 21775136, and 21771158), the Natural Science Foundation of Jiangsu Province (BK20221406), Jiangsu Key Research and Development Project for Social Development Program (BE2022772), and CAS “Light of west China” Program. The authors thank Prof. Ning Xu from the Department of Physics, Yancheng Institute of Technology, Yancheng, China, for the help of density functional theory calculation.

Appendix A. Supporting information

Supplementary data associated with this article can be found in the online version at doi:10.1016/j.apcatb.2024.123806.

References

- [1] K. Yu, T.Y. Zhang, Y.M. Wang, J. Wu, H. Huang, K. Yin, F. Liao, Y. Liu, Z.H. Kang, Anchoring Co_3O_4 on CdZnS to accelerate hole migration for highly stable photocatalytic overall water splitting, Appl. Catal. B: Environ. 324 (2023) 122228.

- [2] L. Yuan, M.Y. Qi, Z.R. Tang, Y.J. Xu, Coupling strategy for CO₂ valorization integrated with organic synthesis by heterogeneous photocatalysis, *Angew. Chem. Int. Ed.* 60 (2021) 21150–22117.
- [3] F. Wang, J. Xu, Z.P. Wang, Y. Lou, Y.F. Zhu, Unprecedentedly efficient mineralization performance of photocatalysis-self-Fenton system towards organic pollutants over oxygen-doped porous g-C₃N₄ nanosheets, *Appl. Catal. B: Environ.* 312 (2022) 121438.
- [4] S. Nishioka, F.E. Osterloh, X.C. Wang, T.E. Mallouk, K. Maeda, Photocatalytic water splitting, *Nat. Rev. Method. Prime.* 3 (2023) 42.
- [5] H. Wang, H.F. Qi, X. Sun, S.Y. Jia, X.Y. Li, T.J. Miao, L.Q. Xiong, S.H. Wang, X. L. Zhang, X.Y. Liu, A.Q. Wang, T. Zhang, W.X. Huang, J.W. Tang, High quantum efficiency of hydrogen production from methanol aqueous solution with PtCu-TiO₂ photocatalysts, *Nat. Mater.* 22 (2023) 619–626.
- [6] L. Luo, L. Fu, H.F. Liu, Y.X. Xu, J.L. Xing, C.R. Chang, D.Y. Yang, J.W. Tang, Synergy of Pd atoms and oxygen vacancies on In₂O₃ for methane conversion under visible light, *Nat. Comm.* 13 (2022) 2930.
- [7] N. Keller, J. Ivanec, J. Highfield, A.M. Ruppert, Photo-/thermal synergies in heterogeneous catalysis: Towards low-temperature (solar-driven) processing for sustainable energy and chemicals, *Appl. Catal. B: Environ.* 296 (2021) 120320.
- [8] R.Y. Zeng, C.C. Cheng, F.S. Xing, Y. Zou, K.N. Ding, C.J. Huang, Dual vacancies induced local polarization electric field for high-performance photocatalytic H₂ production, *Appl. Catal. B: Environ.* 316 (2022) 121680.
- [9] X.H. Jiang, L.S. Zhang, H.Y. Liu, D.S. Wu, F.Y. Wu, L. Tian, L.L. Liu, J.P. Zou, S. L. Luo, B.B. Chen, Silver single atom in carbon nitride catalyst for highly efficient photocatalytic hydrogen evolution, *Angew. Chem. Int. Ed.* 59 (2020) 23112–23116.
- [10] N. Denisov, S.S. Qin, J. Will, B.N. Vasiljevic, N.V. Skorodumova, I.A. Pasti, B. B. Sarma, B. Osuagwu, T. Yokosawa, J. Voss, E. Wirth, P. Schmuki Speecker, Light-Induced agglomeration of single-atom platinum in photocatalysis, *Adv. Mater.* 35 (2023) 2206569.
- [11] Q.J. Mo, L. Zhang, S.H. Li, H.L. Song, Y.N. Fan, C.Y. Su, Engineering single-atom sites into pore-confined nanospaces of porphyrinic metal-organic frameworks for the highly efficient photocatalytic hydrogen evolution reaction, *J. Am. Chem. Soc.* 144 (2022) 22747–22758.
- [12] H.H. Zhai, P.F. Tan, M. Jiang, M.Y. Zhang, R.F. Ren, R.J. Sa, J. Pan, Electronic regulation of Pt single-atom catalysts via local coordination state adjustment for enhanced photocatalytic performance, *ACS Catal.* 13 (2023) 8063–8072.
- [13] J.K. Zhang, Y.K. Pan, D. Feng, L. Cui, S.C. Zhao, J.L. Hu, S. Wang, Y. Qin, Mechanistic insight into the synergy between platinum single atom and cluster dual active sites boosting photocatalytic hydrogen evolution, *Adv. Mater.* 35 (2023) 202300902.
- [14] B. Yang, X.L. Li, Q. Zhang, X.D. Yang, J.G. Wan, G.F. Liao, J.J. Zhao, R.J. Wang, J. C. Liu, R.D. Rodriguez, X. Jia, Ultrathin porous carbon nitride nanosheets with well-tuned band structures via carbon vacancies and oxygen doping for significantly boosting H₂ production, *Appl. Catal. B: Environ.* 314 (2022) 121521.
- [15] P. Kumar, E. Vahidzadeh, U.K. Thakur, P. Kar, K.M. Alam, A. Goswami, N. Mahdi, K. Cui, G.M. Bernard, V.K. Michaelis, K. Shankar, C₃N₄: a low bandgap semiconductor containing an azo-linked carbon nitride framework for photocatalytic, photovoltaic and adsorbent applications, *J. Am. Chem. Soc.* 141 (2019) 5415–5436.
- [16] N. Che, Y. Zeng, T. Li, P.X. Cui, D.D. Dionysiou, X.L. Wang, C. Liu, G.D. Fang, C. C. Ding, Y. Zhao, J. Gao, Y.J. Wang, D.M. Zhou, Phosphorus doping significantly enhanced the catalytic performance of cobalt-single-atom catalyst for peroxymonosulfate activation and contaminants degradation, *J. Hazard. Mater.* 454 (2023) 131480.
- [17] J.L. Zhang, Z. Li, J. He, H.C. Tao, M.S. Chen, Y.T. Zhou, M.S. Zhu, Reinforced photogenerated electrons in few-layer C₃N₄ for enhanced catalytic NO oxidation and CO₂ reduction, *ACS Catal.* 13 (2023) 785–795.
- [18] T.Y. Liu, G.J. Yang, W. Wang, C.X. Wang, M. Wang, X.N. Sun, P. Xu, J.T. Zhang, Preparation of C₃N₅ nanosheets with enhanced performance in photocatalytic methylene blue (MB) degradation and H₂-evolution from water splitting, *Environ. Res.* 188 (2020) 109741.
- [19] C. Peng, L.X. Han, J.M. Huang, S.Y. Wang, X.H. Zhang, H. Chen, Comprehensive investigation on robust photocatalytic hydrogen production over C₃N₅, *Chin. J. Catal.* 43 (2022) 410–420.
- [20] J. Xu, L.W. Zhang, R. Shi, Y.F. Zhu, Chemical exfoliation of graphitic carbon nitride for efficient heterogeneous Photocatalysis, *J. Mater. Chem. A* 1 (2013) 14766–14772.
- [21] L.Z. Wu, X.Y. Yang, T. Chen, Y. Li, Q. Meng, L. Zhu, W.K. Zhu, R. He, T. Duan, Three-dimensional C₃N₅/RGO aerogels with enhanced visible-light response and electron-hole separation efficiency for photocatalytic uranium reduction, *Chem. Eng. J.* 427 (2022) 131773.
- [22] T. Li, P.X. Cui, X.L. Wang, C. Liu, Y. Zeng, G.D. Fang, Y. Zhao, J. Gao, Y.J. Wang, D. M. Zhou, Efficient activation of peroxymonosulfate by C₃N₅ doped with cobalt for organic contaminant degradation, *Environ. Sci. Nano* 9 (2022) 2534–2547.
- [23] J.L. Zhang, H.C. Tao, S.S. Wu, J.L. Yang, M.S. Zhu, Enhanced durability of nitric oxide removal on TiO₂ (P25) under visible light: enabled by the direct Z-scheme mechanism and enhanced structure defects through coupling with C₃N₅, *Appl. Catal. B: Environ.* 296 (2021) 120372.
- [24] L.X. Han, J.M. Huang, J. Zhan, X.H. Zhang, S.Y. Wang, H. Chen, Construction of highly dispersed Ni sites on N-rich carbon nitride for enhanced photocatalytic NO removal, *Adv. Sustain. Syst.* 1 (2022) 2200009.
- [25] J.J. Liu, C.C. Zhao, J.T. Zheng, M.S. Siddique, H.K. Yang, W.Z. Yu, Efficiently photocatalysis activation of peroxydisulfate by Fe-doped g-C₃N₅ for pharmaceuticals and personal care products degradation, *Environ. Pollut.* 322 (2023) 121182.
- [26] L.N. Du, B. Gao, S. Xu, Q. Xu, Strong ferromagnetism of g-C₃N₄ achieved by atomic manipulation, *Nat. Commun.* 14 (2023) 2278.
- [27] Y.H. Li, J. Xing, Z.J. Chen, Z. Li, F. Tian, L.R. Zheng, H.F. Wang, P. Hu, H.J. Zhao, H.G. Yang, Unidirectional suppression of hydrogen oxidation on oxidized platinum clusters, *Nat. Commun.* 4 (2013) 2500.
- [28] C.J. Li, J.L. Zhang, X.L. Chen, H.C. Tao, Y.T. Zhou, M.S. Zhu, Upgraded charge transfer by an internal electric field in 2D/2D BiOCl/N-rich C₃N₅ heterojunctions for efficiently visible-light catalytic NO removal, *Chem. Eng. J.* 468 (2023) 143753.
- [29] H. Wang, M. Li, Q. Lu, Y. Cen, Y. Zhang, S. Yao, A mesoporous rod-like g-C₃N₅ synthesized by salt-guided strategy as a superior photocatalyst for degradation of organic pollutant, *ACS Sustain. Chem. Eng.* 7 (2019) 625–631.
- [30] C. Fu, M.Y. Zhao, X. Chen, G.W. Sun, C. Wang, Q.J. Song, Unraveling the dual defect effects in C₃N₅ for piezo-photocatalytic degradation and H₂O₂ generation, *Appl. Catal. B: Environ.* 332 (2023) 122752.
- [31] D. Liu, S.T. Chen, Y.X. Zhang, R.J. Li, T.Y. Peng, Modulating the bridging units of carbon nitride for highly efficient charge separation and visible-light-responsive photocatalytic H₂ evolution, *Appl. Catal. B: Environ.* 333 (2023) 122805.
- [32] N. Daelman, M. Capdevila-Cortada, N. López, Dynamic charge and oxidation state of Pt/CeO₂ single-atom catalysts, *Nat. Mater.* 18 (2019) 1215–1221.
- [33] J. Li, Q.Y. Zhou, M.F. Yue, S.G. Chen, J.H. Deng, X.Y. Ping, Y. Li, J. Li, Q. Liao, M. H. Shao, Z.D. Wei, Cross-linked multi-atom Pt catalyst for highly efficient oxygen reduction catalysis, *Appl. Catal. B: Environ.* 284 (2021) 119828.
- [34] X.F. Yang, A.Q. Wang, B.T. Qiao, J. Li, J.Y. Liu, T. Zhang, Single-atom catalysts: a new frontier in heterogeneous catalysis, *Acc. Chem. Res.* 46 (2013) 1740–1748.
- [35] Y.F. Chen, Z.J. Li, Y.B. Zhu, D.M. Sun, X.E. Liu, L. Xu, Y.W. Tang, Atomic Fe Dispersed on N-Doped carbon hollow nanospheres for high-efficiency electrocatalytic oxygen reduction, *Adv. Mater.* 31 (2019) 1806312.
- [36] L.X. Yu, Y. Pan, H.M. Li, R.C. Xu, Z.H. Sun, Highly active and water-resistant Lanthanum-doped platinum-cobalt oxide catalysts for CO oxidation, *Appl. Catal. B: Environ.* 331 (2023) 122678.
- [37] J. Cho, T. Lim, H. Kim, L. Meng, J. Kim, S. Lee, J.H. Lee, G.Y. Jung, K.S. Lee, F. Viñes, F. Illas, K.S. Exner, S.H. Joo, C.H. Choi, Importance of broken geometric symmetry of single-atom Pt sites for efficient electrocatalysis, *Nat. Commun.* 14 (2023) 3233.
- [38] J. Li, P. Liu, Y.Z. Tang, H.L. Huang, H.Z. Cui, D.H. Mei, C.L. Zhong, Single-atom Pt–N₃ sites on the stable covalent triazine framework nanosheets for photocatalytic N₂ fixation, *ACS Catal.* 10 (2020) 2431–2442.
- [39] T. Lim, G.Y. Jung, J.H. Kim, S.O. Park, J. Park, Y.T. Kim, S.J. Kang, H.Y. Jeong, S. K. Kwak, S.H. Joo, Atomically dispersed Pt-N₄ sites as efficient and selective electrocatalysts for the chlorine evolution reaction, *Nat. Commun.* 11 (2020) 412.
- [40] J. Yang, W.G. Liu, M.Q. Xu, X.Y. Liu, H.F. Qi, L.L. Zhang, X.F. Yang, S.S. Niu, D. Zhou, Y.F. Liu, Y. Su, J.F. Li, Z.Q. Tian, W. Zhou, A.Q. Wang, T. Zhang, Dynamic behavior of single-atom catalysts in electrocatalysis: identification of Cu-N₃ as an active site for the oxygen reduction reaction, *J. Am. Chem. Soc.* 143 (2021) 14530–14539.
- [41] W. Maneprakorn, M.A. Malik, P. O'Brien, Developing chemical strategies for the assembly of nanoparticles into mesoscopic objects, *J. Am. Chem. Soc.* 6 (2010) 1780–1781.
- [42] G. Liu, T. Wang, H. Zhang, X. Meng, D. Hao, K. Chang, P. Li, T. Kako, J. Ye, Nature-inspired environmental “phosphorylation” boosts photocatalytic H₂ production over carbon nitride nanosheets under visible-light irradiation, *Angew. Chem. Int. Ed.* 54 (2015) 13561–13565.
- [43] L.W. Zhang, R. Long, Y.M. Zhang, D.L. Duan, Y.J. Xiong, Y.J. Zhang, Y.P. Bi, Direct observation of dynamic bond evolution in single-atom Pt/C₃N₄, *Catal. Angew. Chem. Int. Ed.* 59 (2020) 6224–6229.
- [44] K. Ito, K. Noda, Highly efficient hydrogen production and selective CO₂ reduction by C₃N₅ photocatalyst using only visible light, *Phys. Chem. Chem. Phys.* (2023), <https://doi.org/10.1039/D3CP04431A>.
- [45] S.F. Ng, X.Z. Chen, J.J. Foo, M. Xiong, W.J. Ong, 2D carbon nitrides: regulating non-metal boron-doped C₃N₅ for elucidating the mechanism of wide pH range photocatalytic hydrogen evolution reaction, *Chin. J. Catal.* 47 (2023) 150–1160.
- [46] Q.J. Shi, Z.J. Li, L. Chen, X.L. Zhang, W.H. Han, M.Z. Xie, J.L. Yang, L.Q. Jing, Synthesis of SPR Au/BiVO₄ quantum dot/rutile-TiO₂ nanorod array composites as efficient visible-light photocatalysts to convert CO₂ and mechanism insight, *Appl. Catal. B: Environ.* 244 (2019) 641–649.
- [47] M. Afkari, S.M. Masoudpanah, M. Hasheminiyari, S. Alamolhoda, Effects of iron oxide contents on photocatalytic performance of nanocomposites based on g-C₃N₄, *Sci. Rep.* 13 (2023) 6203.
- [48] Z. Lu, L. Zeng, W.L. Song, Z.Y. Qin, D.W. Zeng, C.S. Xie, In situ synthesis of C-TiO₂/g-C₃N₄ heterojunction nanocomposite as highly visible light active photocatalyst originated from effective interfacial charge transfer, *Appl. Catal. B: Environ.* 202 (2017) 489–499.
- [49] C. Zhao, Z. Chen, J. Xu, Q. Liu, H. Xu, H. Tang, G. Li, Y. Jiang, F. Qu, Z. Lin, X. Yang, Probing supramolecular assembly and charge carrier dynamics toward enhanced photocatalytic hydrogen evolution in 2D graphitic carbon nitride nanosheets, *Appl. Catal. B: Environ.* 256 (2019) 117867.
- [50] Y.H. Su, Z.H. Wei, Y.B. Lian, Q.Q. Mu, W.Y. Pan, D.Q. Song, Y.Z. Qin, W. Hua, J. Cheng, Z. Deng, Y. Peng, Defect-driven electroless deposition and activation of platinum sites on ZnIn₂S₄ nanosheets for accelerated kinetics of photocatalytic hydrogen production, *Appl. Catal. B: Environ.* 334 (2023) 122827.
- [51] Y.B. Zhao, P. Zhang, Z.C. Yang, L.N. Li, J.Y. Gao, S. Chen, T.F. Xie, C.Z. Diao, S. B. Xi, B.B. Xiao, C. Hu, W.Y. Choi, Mechanistic analysis of multiple processes controlling solar-driven H₂O₂ synthesis using engineered polymeric carbon nitride, *Nat. Commun.* 12 (2021) 3701.

- [52] L.H. Xia, K.S. Zhang, X.D. Wang, Q. Guo, Y.N. Wu, Y.J. Du, L.X. Zhang, J.F. Xia, H. Tang, X. Zhang, Y.H. Peng, Z. Li, X.L. Yang, 0D/2D Schottky junction synergies with 2D/2D S-scheme heterojunction strategy to achieve uniform separation of carriers in 0D/2D/2D quasi CNQDs/TCN/ZnIn₂S₄ towards photocatalytic remediating petroleum hydrocarbons polluted marine, *Appl. Catal. B: Environ.* 325 (2023) 122387.
- [53] X.D. Zhu, Z.M. Song, Z.Y. Wang, W. Liu, B. Hong, J. Bao, C. Gao, S. Sun, Selective formation of interfacial bonding enables superior hydrogen production in organic-inorganic hybrid cocatalyzed photocatalysts, *Appl. Catal. B: Environ.* 274 (2020) 119010.
- [54] C.Q. Xu, H.Y. Liu, D.Y. Wang, D.Z. Li, Y. Zhang, X.L. Liu, J.Y. Huang, S.Q. Wu, D. H. Fan, H.G. Liu, H. Pan, Molten-salt assisted synthesis of polymeric carbon nitride-based photocatalyst for enhanced photocatalytic activity under green light irradiation, *Appl. Catal. B: Environ.* 334 (2023) 122835.
- [55] R. Abe, K. Sayama, H. Arakawa, Significant effect of iodide addition on water splitting into H₂ and O₂ over Pt-loaded TiO₂ photocatalyst: suppression of backward reaction. *Chem. Phys. Lett.* 371 (2003) 360–364.
- [56] X.M. Yang, J.W. Cui, X.L. Liu, Q.Q. Zhang, D.F. Wang, J.H. Ye, L.Q. Liu, Boosting photocatalytic overall water splitting over single-layer graphene coated metal cocatalyst, *Appl. Catal. B: Environ.* 325 (2023) 122369.
- [57] Z. Li, R.G. Li, H.J. Jing, J.P. Xiao, H.C. Xie, F. Hong, N. Ta, X.W. Zhang, J. Zhu, C. Li, Blocking the reverse reactions of overall water splitting on a Rh/GaN-ZnO photocatalyst modified with Al₂O₃, *Nat. Catal.* 6 (2023) 80–88.
- [58] B.W. He, P. Xiao, S.J. Wan, J.J. Zhang, T. Chen, L.Y. Zhang, J.G. Yu, Rapid charge transfer endowed by interfacial Ni-O bonding in s-scheme heterojunction for efficient photocatalytic H₂ and imine production, *Angew. Chem. Int. Ed.* 62 (2023) e202313172.
- [59] A. Michaelides, P. Hu, Catalytic water formation on platinum: a first-principles study, *J. Am. Chem. Soc.* 123 (2001) 4235–4242.
- [60] S.C. Sun, Y.B. Feng, L. Pan, X.W. Zhang, J.J. Zou, Integrating Pt@Ni(OH)₂ nanowire and Pt nanoparticle on C₃N₄ with fast surface kinetics and charge transfer towards highly efficient photocatalytic water splitting, *Appl. Catal. B: Environ.* 259 (2019) 118028.